frontiers | Frontiers in Earth Science

TYPE Original Research
PUBLISHED 13 January 2023
DOI 10.3389/feart.2022.1046122

Late Paleozoic tectonics of Southern Central Asian orogenic belt: Evidence from magmatic rocks in the northern Alxa, Northwest China

Er-Teng Wang[1], Xin-Wei Zhai[1]*, Wan-Feng Chen[1], Zhen Ma[2], Lei Wu[1], Zhi-Ang Guo[1], Yun Wang[1], Gao-Rui Song[1] and Jin-Rong Wang[1]

[1]Key Laboratory of Mineral Resources in Western China (Gansu Province), School of Earth Science, Lanzhou University, Lanzhou, China, [2]Ningxia Survey and Monitoring Institute of Land Resources, Yinchuan, Ningxia, China

Check for updates

OPEN ACCESS

EDITED BY
Zhong-Hai Li,
University of Chinese Academy of Sciences, China

REVIEWED BY
Gaoxue Yang,
Chang'an University, China
Xuxuan Ma,
Chinese Academy of Geological Sciences, China

*CORRESPONDENCE
Xin-Wei Zhai,
zhaixw926@lzu.edu.cn

SPECIALTY SECTION
This article was submitted to Structural Geology and Tectonics, a section of the journal Frontiers in Earth Science

RECEIVED 16 September 2022
ACCEPTED 31 October 2022
PUBLISHED 13 January 2023

CITATION
Wang E-T, Zhai X-W, Chen W-F, Ma Z, Wu L, Guo Z-A, Wang Y, Song G-R and Wang J-R (2023), Late Paleozoic tectonics of Southern Central Asian orogenic belt: Evidence from magmatic rocks in the northern Alxa, Northwest China.
Front. Earth Sci. 10:1046122.
doi: 10.3389/feart.2022.1046122

Late Paleozoic magmatic rock outcrops are common in the Northern Alxa, Southern Central Asian Orogenic Belt (CAOB), which is a key area for understanding tectonic processes and defining the final closure time of the Paleo-Asian Ocean (PAO). We present zircon U–Pb chronology and whole-rock geochemistry data for late Paleozoic magmatic rocks from the Yagan area of northern Alxa. This paper reveals two periods of magmatism: syenogranite (374.8 Ma) and bimodal intrusive rocks, which consist of gabbro (261.4 Ma), diabase (262.9 Ma) and biotite monzogranite (263.4 Ma). The syenogranite is high-K calc-alkaline and shows enrichments in Th, Zr, Hf and LREEs; depletions in Sr, Nb, Ta, and Ti; and low Mg# values (6.9–13.2); the syenogranite was derived from partial melting of the crust and has volcanic arc characteristics. The gabbro and diabase have similar geochemical characteristics, such as enrichments in Pb, Rb, Sr, Zr, and Hf and depletions in Nb, Ta, and Ti, with positive $\varepsilon_{Hf}(t)$ values (+0.9–+2.7 and +2.6–+3.6, respectively), indicating that they originated from partial melting of depleted mantle and experienced crustal contamination during magma emplacement. The biotite monzogranite shows depletions in Nb, Ta, and Ti and ε_{Nd} (t) values of -2.6 to –2.4 and resulted from partial melting of the lower crust caused by asthenospheric underplating. The bimodal intrusive rocks formed in a postcollision extensional setting. Combined with previous data, we conclude that northern Alxa was an active continental margin during the late Devonian and that the final closure of the Yagan branch ocean of the PAO occurred prior to the middle Permian.

KEYWORDS

granite, bimodal intrusive rocks, late Paleozoic, tectonics, northern Alxa, Central Asian orogenic belt

1 Introduction

The Central Asian Orogenic Belt (CAOB), one of the largest Phanerozoic accretionary orogenic belts in the world, is situated between the Siberian and Tarim craton (Figure 1A) and composed of a large number of accretionary complexes, arcs, ophiolites, oceanic plateaus and terranes, and its tectonic evolution was triggered by the breakup of Rodinia and the subduction and closure of the Paleo-Asian Ocean (PAO) during the Neoproterozoic to late Paleozoic (Sengör et al., 1993; Jahn et al., 2000; Windley et al., 2007; Xiao et al., 2009; Yang et al., 2015, 2020; Song et al., 2021). Until now, there are vigorous controversies about the timing of the final closure of the PAO. The final closure might have occurred in the middle Devonian (Su et al., 2011; Li et al., 2013; Xu et al., 2013), before the late Carboniferous (Xia et al., 2012; Li et al., 2022), before the early Permian (Xie et al., 2020), during the late Permian to early Triassic (Xiao et al., 2018; Li et al., 2020) or the in Triassic (Song et al., 2021).

The Alxa area is located in the central southern CAOB (Figure 1A). Prior studies have shown that the Enger Us and Quagan Qulu faults (ophiolitic belts) (Figure 1B) in the Alxa area are the lithospheric remnants of the ancient ocean and back-arc basin between the Tarim and North China cratons, respectively (Wang et al., 1993; Wu & He, 1993), but according to recent findings, both have been linked to the tectonic evolution of the PAO (Zhang et al., 2013; Song et al., 2017; Li et al., 2020; Zhao et al., 2020; Hui et al., 2021) and are currently accepted as the product of the final closure of the PAO (Zheng et al., 2017). Therefore, the Alxa area is a pivotal area for investigating the tectonic relationship of the timing of the final closure of the PAO and the tectonic evolution of the southern CAOB. However, the tectonic evolution of northern Alxa has long been controversial, and different opinions are as follows: 1) the late Paleozoic

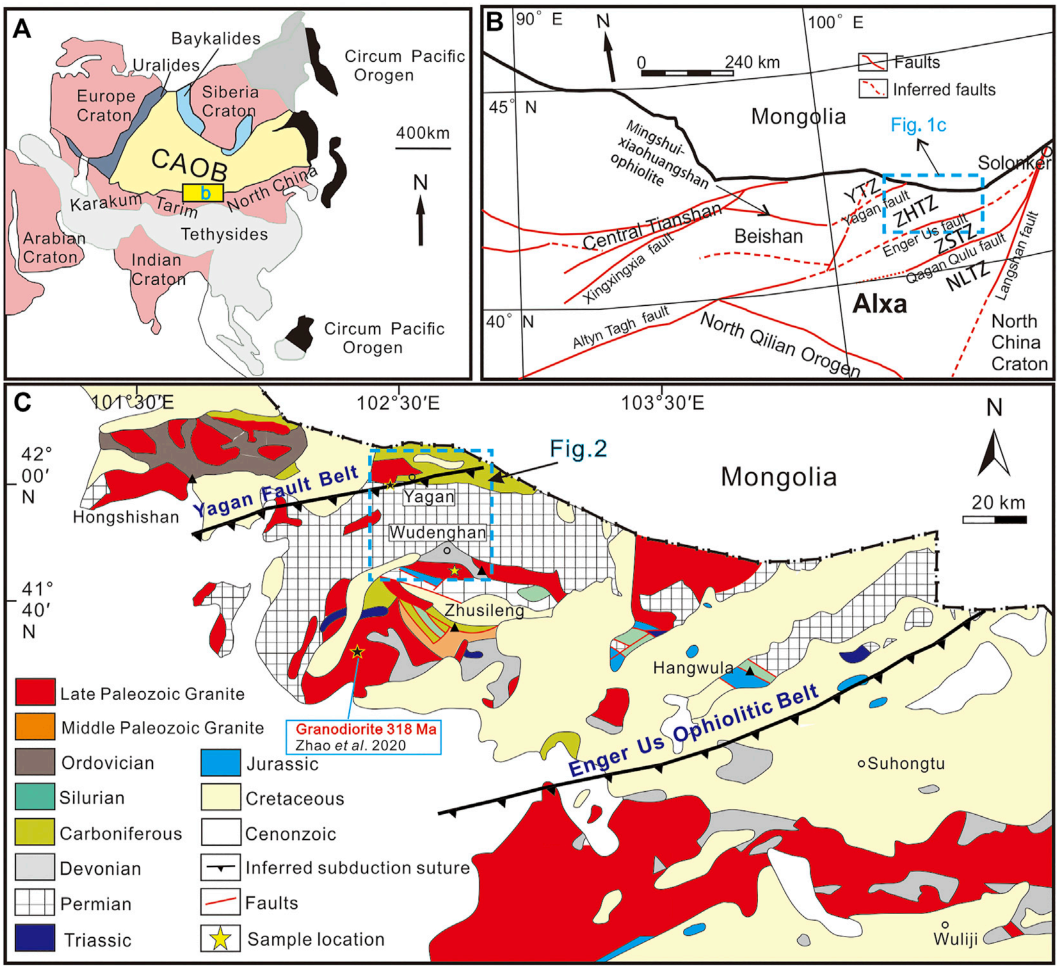

FIGURE 1
(A) Geological map of the Central Asian Orogenic Belt (modified after Jahn et al., 2000). **(B)** Tectonic units of Alxa block (modified after Wu & He, 1993). **(C)** Geological map of the northern Alxa region (modified after Shi et al., 2011). YTZ: Yagan tectonic zone, ZHTZ: Zhusileng-Hangwula tectonic zone, ZSTZ: Zongnaishan-Shalazhashan tectonic zone, NLTZ: Nuru-Langshan tectonic zone.

magmatic activity in the Zhusileng–Hangwula tectonic zone (ZHTZ) (Figure 1C) was related to the southward subduction of the Yagan branch ocean of the PAO, represented by the Yagan fault (Wang et al., 1992; Zheng et al., 2013; Song et al., 2017), or the northward subduction of the PAO, represented by the Enger Us ophiolitic belt (Liu et al., 2018; Xie et al., 2020; Zhao et al., 2020); this system shows that the geodynamic transformation mechanism of northern Alxa changed from a passive continental margin to an active continental margin. However, the geological features show that the Enger Us ophiolite belt is southward subducted (Wang et al., 1992), and the Zongnaishan–Shalazhashan zone (Figure 1B) is a volcanic arc (Wang et al., 1994). 2) Northern Alxa was a subduction setting during the late Devonian to late Carboniferous (Zhao et al., 2020) or early Permian (Liu et al., 2017) or a postcollision extensional setting during the early Permian (Zheng et al., 2021). 3) The timing of the final closure time of the PAO in the Alxa region was during the Early Devonian (Liu et al., 2018), before the early Permian (Fei et al., 2019), from the Permian to early–middle Triassic (Li et al., 2020) or during the middle–late Triassic (Song et al., 2021).

In any case, there are remained debated for geotectonic framework during the late Paleozoic and the final closure of the PAO in the northern Alxa (Xie et al., 2020; Zhao et al., 2020). To promote our understanding of the above debate, this study presents zircon U-Pb ages and whole-rock major- and trace-element and Nd-Hf isotope data of the late Paleozoic syenogranite, gabbro, diabase and biotite monzogranite in the Yagan area of northern Alxa and discusses their petrogenesis and the implications for the tectonic evolution of the southern CAOB.

2 Geological backgrounds

The Alxa region is between the Beishan-Tianshan orogenic belt to the west and the north Qilian orogenic belt to the south (Figure 1B). In the Alxa block, three major faults/ophiolite belts, the Yagan fault, Enger Us ophiolite belt and Quagan Qulu ophiolite belt (Figure 1B), and it is divided into southern and northern parts by the Enger Us ophiolite belt, and the Yagan area is part of the northern Alxa region (Figure 1C) and covers the Yagan tectonic zone (YTZ) in the north, the ZHTZ in the south (Figure 1B). The YTZ is located to the north of the Yagan fault belt (Figure 1B). The Paleozoic volcano-sedimentary strata, magmatic activities and ophiolite are distributed mainly in the Alxa region. The Enger Us ophiolite belt is the major suture zone of the PAO in the Alxa (Wu & He, 1993; Zheng et al., 2014).

The geology of the areas surrounding northern Alxa indicates a significant change in the tectonic setting, as evidenced by the existence of lower and upper Paleozoic strata. The lower Paleozoic strata are a normal depositional sequence and are composed of Cambrian–lower Ordovician siliceous rock, silty dolomite, silt–slate and crystalline limestone and lower Silurian argillaceous slate, siliceous slate and tuffaceous sandstone; the strata are deep-sea facies clastic rocks that are mainly distributed in the ZHTZ, indicating shallow marine and carbonate sequences in a passive continental margin (Wu & He, 1993). Moreover, minor Upper Devonian limestones, sandstones, andesites and andesitic tuffs (Zhao et al., 2020) are distributed in the Yagan region. The upper Paleozoic strata in northern Alxa are composed of marine volcanic rocks and deep-sea flysch formations (Yin, 2016), such as Carboniferous feldspar-containing sandstone and conglomerate, limestone, andesite and tuff and Permian limestone, pyroclastic rocks and volcaniclastic rocks, indicating that strong magmatic activity occurred in this period. In summary, a great tectonic transformation, e.g., from a passive continental margin to an active continental margin, occurred in the northern area during the late Paleozoic (Wang et al., 1994; Zhao et al., 2020).

The magmatic activities of northern Alxa show the characteristics of the subduction arc during the late Paleozoic, which was resulted from the subduction of the PAO (Zhao et al., 2020; Hui et al., 2021). While other research suggests that the early Permian magmatic activities in the northern Alxa are related to Tarim large igneous province (Dan et al., 2014). Yet studies show the Carboniferous-Permian bimodal volcanic rocks in this area were formed in the post-collision extensional tectonic setting (Xie et al., 2020). The Enger Us ophiolite belt is composed of ultramafic and basic rocks, and produced by tectonic melange zone, which is geochemical characterized of N–MORB (Zheng et al., 2014), it is believed a suture between the Tarim and the North China Plate (Wang et al., 1994). Except for the olivine gabbro near the Yagan fault belt, ophiolite mélange does not occur along the belt (Zheng et al., 2013), but the Yagan fault would be an eastward extension of the Mingshui-Xiaohuangshan ophiolite belt (Figure 1B) in the Beishan region of the southern CAOB (Wu et al., 1998). To sum up, the study of magma activity in the northern Alxa has guiding significance in tectonic framework of southern CAOB.

3 Samples descriptions

For this study, syenogranite samples were collected from the Wudenghan batholith (Figure 2). The syenogranite is light red in color (Figure 3A) with medium to coarse porphyritic texture. The phenocrysts are mainly potassium feldspar (25%), and the matrix is composed of quartz (30%), plagioclase (20%), potassium feldspar (15%), biotite (6%), minor amphibole (3%) and magnetite (1%). Feldspar and plagioclase are euhedral to subhedral. Biotite and amphibole are subhedral (Figures 3B,C). The diabase, gabbro and biotite monzogranite samples were collected from the Yagan batholith in the south Yagan fault (Figure 2). They outcrop in dikes and intrude into the sandy slate, marble and gneiss strata of Devonian (Figure 2B). The diabase samples are grayish-green (Figure 3D) and have an ophitic

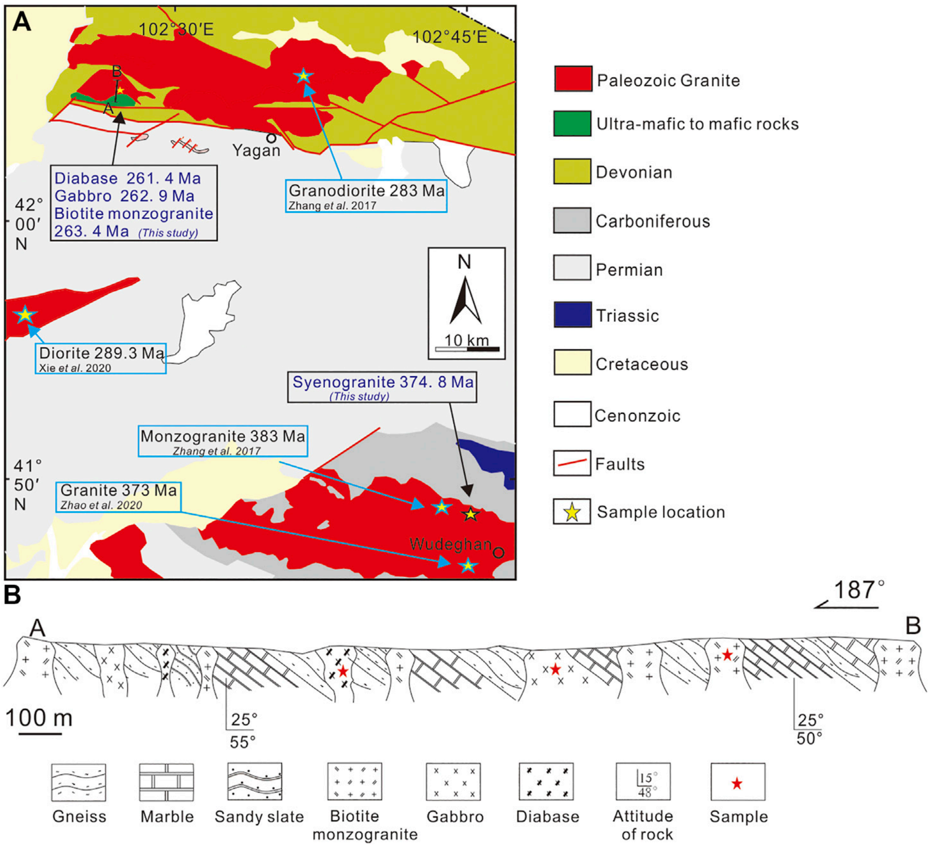

FIGURE 2
(A) Geological map of the studied area (Modified after 1:200,000 geological maps, Inner Mongolian Bureau of Geology and Mineral Resources, China); **(B)** Profile of the Yagan bimodal intrusive rocks.

texture (Figure 3F). They are composed of plagioclase (65%), pyroxene (25%), minor olivine (5%) and opaque minerals (5%) (Figures 3E,F). The diabase is strongly altered indicating by the highly chloritized pyroxene (Figure 3F). The gabbro samples are light gray and contain plagioclase (50%), monoclinic pyroxene (15%–20%), amphibole (20%), minor (10%) sphene and chlorite (Figures 3G–I). The biotite monzonite samples are gray and massive (Figure 3J). Their assemblages include plagioclase (35%), potassium feldspar (20%), quartz (30%), biotite (10%) and minor amphibole (5%). The plagioclase is subhedral and has been altered. The amphibole is subhedral, and some of it fills quartz voids. The biotite is subhedral and occurs in chloritization (Figure 3K and L).

4 Analytical methods

Zircon cathodoluminescence (CL) images were obtained at the Langfang Chenxin Geological Service Co., Hebei, China. U-Pb dating, whole-rock major, trace element and Nd-Hf isotope analyses were performed at the Key Laboratory of Mineral Resources in Western China, Lanzhou University, Lanzhou, China.

4.1 Zircon U-Pb dating

After separation by conventional heavy liquid and magnetic techniques, zircon grains were hand-picked and embedded in an epoxy mount under a binocular microscope and then polished to expose half of the zircon grains. The zircon grains with internal ring structures, no clear inclusions and fewer fractures in the CL, transmitted and reflected images were chosen as suitable targets for U-Pb dating. The U-Pb isotope ratios of the selected zircons were measured using an Agilent 7500X ICP-MS instrument combined with a Geo-Las200M laser ablation (LA) system. The zircon standard 91500 (Wiedenbeck et al., 1995) was used as the age standard. The reference glass NIST 610 (Andersen, 2002) and Si were applied as external and internal standards, respectively, during the process of analyzing the

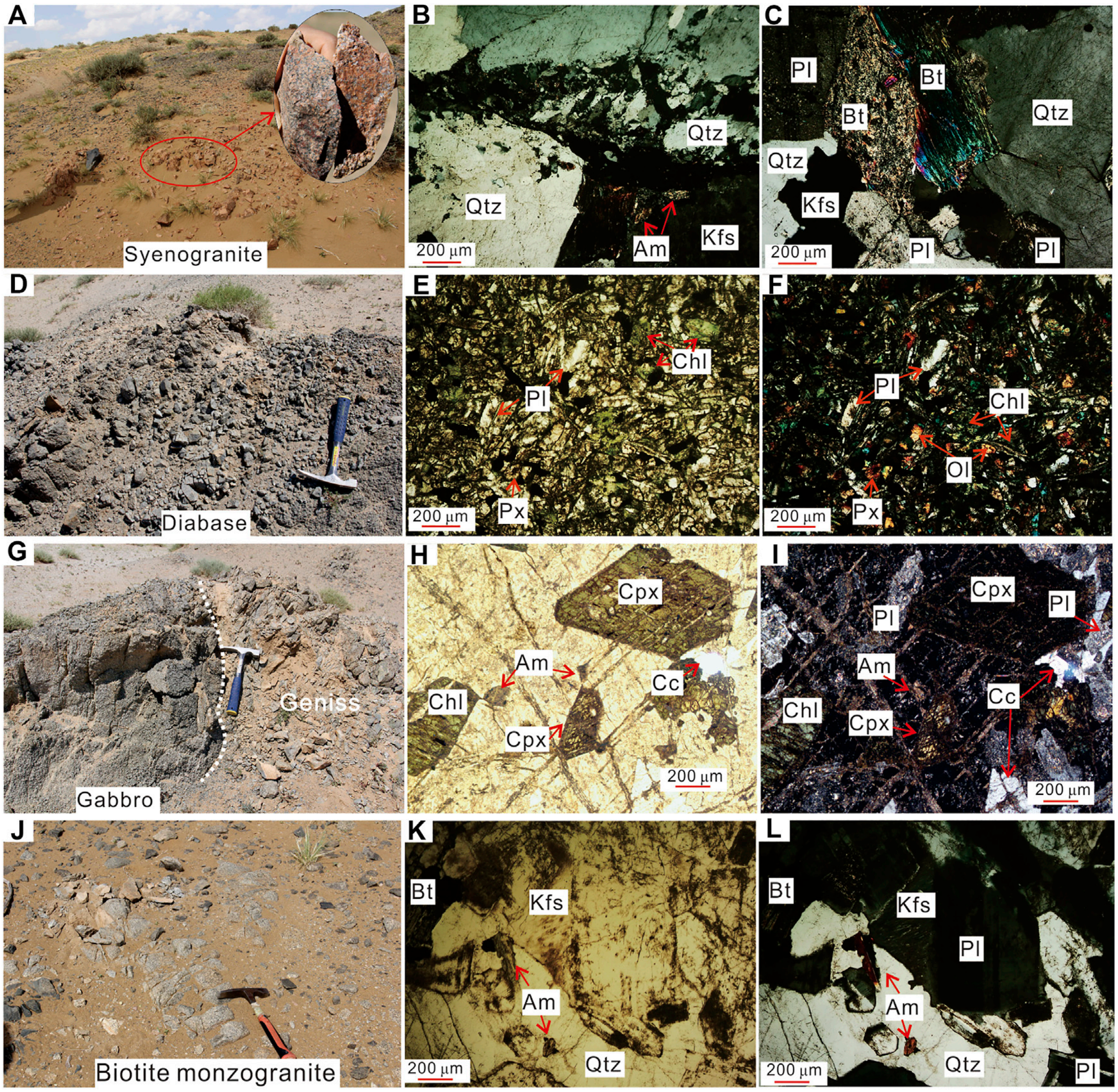

FIGURE 3
Field outcrops and microphotographs **(A–C)** Syenogranite **(D–F)** Diabase **(G–I)** Gabbro **(J–L)** Biotite monzogranite. Abbreviation: Am–amphibole; Cc–calcite; Cpx–clinopyroxene; Chl–chlorite; Ol–olivine; Pl–plagioclase; Qtz–Quartz; Kfs–K-feldspar; Bt–biotite; Zr–Zircon.

elemental composition of the zircon. The spot diameter was ~30 μm and the analytical techniques are referred to Luan et al. (2019). Data reduction was performed using the Glitter (ver. 4.0) program, and common Pb was corrected using the common lead correction program (ver. 3.15; Andersen, 2002). Concordia plots and weighted mean ages were generated using the Isoplot program (ver. 3.0; Ludwig, 2003).

4.2 Major and trace element analyses

Major element compositions were analyzed by ICP optical emission spectroscopy (ICP-OES). The analytical accuracy was better than 2%. The loss on ignition (LOI) was obtained by heating approximately 0.5 g of dried sample powder at 1000°C for 2 h. Trace element contents were analyzed by ICP-MS on an Agilent 7700X instrument, and the analytical errors were less than 10%. The US Geological Survey reference materials AGV-2 and BCR-2 were used as standards.

4.3 Whole-rock Nd-Hf isotopes

Sample rock powders were mixed with 0.5 ml 60 wt% HNO_3 and 1.0 ml 40 wt% HF in high-pressure PTFE bombs. These bombs were steel-jacketed and placed in the oven at 195°C for

FIGURE 4
Representative zircons cathodoluminescence (CL) images for syenogranite, diabase, gabbro and biotite monzogranite in the Yagan area of northern Alxa.

3 days. Digested samples were dried on a hotplate and reconstituted in 1.5 ml of 1.5 N HCl before ion exchange purification. The analytical procedure was the same as that described by Liang et al. (2002). The diluted solution (50 ppb Nd, 40 ppb Hf) was introduced into a Nu Instruments Nu Plasma II MC-ICP-MS (Wrexham, Wales, United Kingdom) through a Teledyne Cetac Technologies Aridus II desolating nebulizer system (Omaha, Nebraska, United States). Raw data of the isotopic ratios were internally corrected for mass fractionation by normalizing to $^{146}Nd/^{144}Nd = 0.7219$ for Nd and $^{179}Hf/^{177}Hf = 0.7325$ for Hf with the exponential law. International isotopic standards (JNdi-1 for Nd, Alfa Hf for Hf) were periodically analyzed to correct instrumental drift. Geochemical reference materials of USGS BCR-2, AVG-2, were treated as quality control.

5 Results

5.1 Zircon U-Pb ages

The zircon U-Pb data of syenogranite (YG-32), diabase (YG-6), gabbro (YG-16) and biotite monzogranite (YG-11) are listed in Supplementary Table S1.

The zircon grains from the syenogranite samples are subhedral and short columnar in shape, with aspect ratios of 1.5:1. The clear oscillatory zone texture (Figure 4) and high Th/U ratios (0.43–1.27) indicate a typical magmatic origin (Wu & Zheng, 2004). Twenty-five spots for the syenogranite samples were analyzed. Five spots (YG32-1, 2, 10, 15, and 17) were excluded from their age calculation because of the high discordance (Supplementary Table S1). The $^{206}Pb/^{238}U$ age of the YG32-14 spot is 1168 ± 12 Ma, indicating captured zircons. The other fifteen spots yielded concordant $^{206}Pb/^{238}U$ ages from 367 ± 4 Ma to 382 ± 4 Ma, with a weighted mean of $^{206}Pb/^{238}U$ of 374.8 ± 3.0 Ma (MSWD = 1.8) (Figure 5), representing the crystallization age of syenogranite.

The zircon grains from the diabase samples are euhedral to subhedral and columnar, with length-to-width ratios of 1:1–3:1. The zircon exhibits oscillatory zoning in the CL images (Figure 4). Twenty-two spots were analyzed and they have high Th/U ratios (0.36–0.98), indicative of a magmatic origin (Wu & Zheng, 2004). Five spots (YG6-3, 5, 13, 15, 19 and 21) were excluded from the age calculation because of the high discordance (Supplementary Table S1). Four zircon core (YG6-7, 10, 18, and 20) analyses yielded concordant $^{207}Pb/^{206}Pb$ ages of 1650 Ma and 881 Ma, indicating captured zircons. Eleven spots yielded concordant $^{206}Pb/^{238}U$ ages from 256 ± 3 Ma to 269 ± 3 Ma, with a weighted mean $^{206}Pb/^{238}U$ of 261.4 ± 3.2 Ma (MSWD = 2.4) (Figure 5), representing the crystallization age of diabase.

The zircon grains from the gabbro samples are subhedral and short columnar, with length to width ratios of 1:1–2:1. Their CL

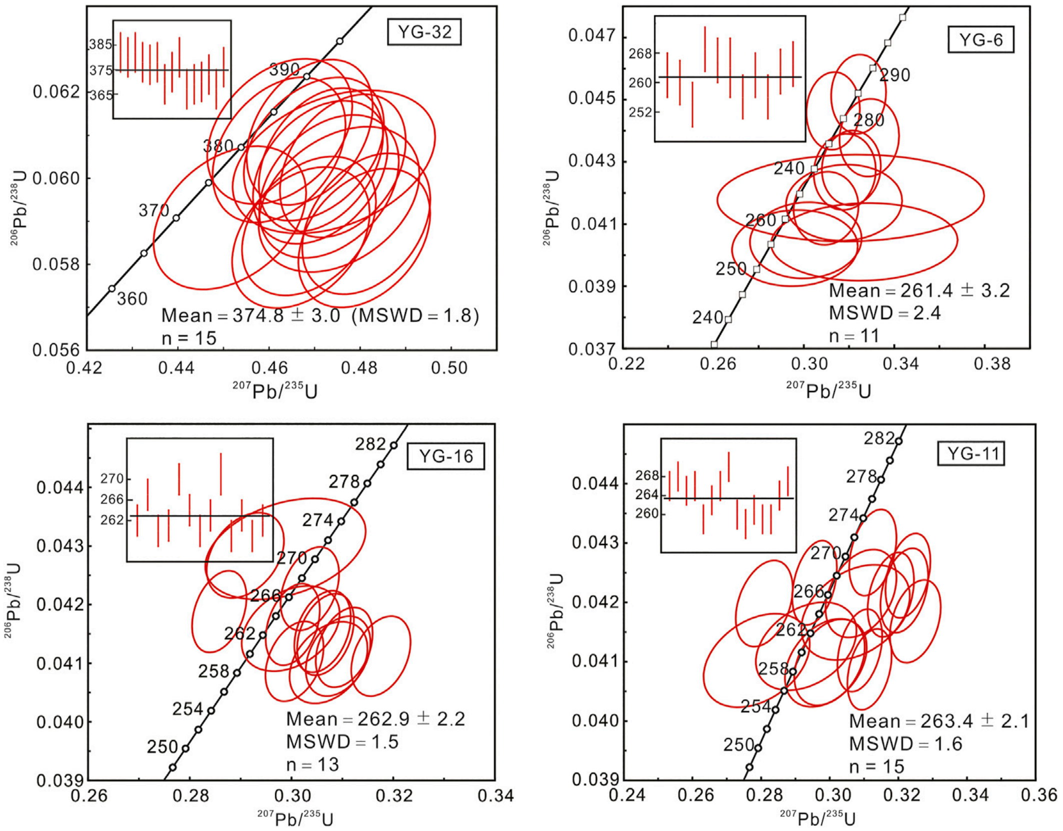

FIGURE 5
Zircon U-Pb concordia diagrams and weighted age from the syenogranite (16 YG-32), diabase (16YG-6), gabbro (16 YG-16) and biotite monzogranite (16 YG-11) in the Yagan area of northern Alxa.

images show clear oscillatory zoning (Figure 4). Additionally, they have high Th/U ratios (0.58–1.23). Fifteen spots for the biotite monzogranite samples were analyzed. One spots (YG16-9) were excluded from the age calculation because of deviation from the concordant curve. One captured zircon (YG16-15) yielded a $^{206}Pb/^{238}U$ age of 413 ± 4 Ma. Thirteen spots yielded concordant $^{206}Pb/^{238}U$ ages from 259 ± 3 Ma to 270 ± 3 Ma, with a weighted mean $^{206}Pb/^{238}U$ of 262.9 ± 2.2 Ma (MSWD = 1.5) (Figure 5), representing the crystallization age of gabbro.

The zircon grains from the biotite monzogranite samples are euhedral to subhedral and columnar, with length-to-width ratios of 3:2–4:1, and they display oscillatory zoning (Figure 4). Their Th/U ratios range from 0.56 to 1.39, which is characteristic of a magmatic origin (Wu & Zheng, 2004). Nineteen spots for the diabase samples were analyzed. Ten spots (YG11-4, 8, 10, 14) were excluded from the age calculation because of their high discordance (Supplementary Table S1). Fifteen spots yielded concordant $^{206}Pb/^{238}U$ ages from 258 ± 3 Ma to 270 ± 3 Ma, with a weighted mean $^{206}Pb/^{238}U$ of 263.4 ± 2.1 Ma (MSWD = 1.6) (Figure 5), representing the crystallization age of biotite monzogranite.

5.2 Major and trace elements

The whole-rock major and trace element data are listed in Supplementary Table S2.

5.2.1 Syenogranite

The samples (16YG28 to 16YG38 in Supplementary Table S2) have high contents of SiO_2 (70.60–73.27 wt%), Na_2O (3.66–4.63 wt%), and K_2O (3.45–4.59 wt%), moderate contents of Al_2O_3 (11.83 - 13.23 wt%), low contents of CaO (1.39–3.14 wt %), MgO (0.11–0.27 wt%) and low $Mg^\#$ values ($Mg^\# = 100*Mg^{2+}/(Mg^{2+} + Fe^{2+})$) of 7–13, and TiO_2 (0.29–0.35 wt%). All samples plot in granite domain and belong to syenogranite (Figure 6A). The syenogranite is characteristic of the metaluminous (Figure 6B) and high-K calc-alkaline series (Figure 6C). On the primitive mantle-normalized trace element variation diagram (Figure 7A), the syenogranite samples show enrichments in large ion lithophile elements (LILEs, e.g., Rb, Ba, K, and Th), weak enrichments in Zr and Hf and depletions in high field strength elements (HFSEs, e.g., Nb, Ta, Ti). Furtherly, the samples are enriched in light REEs (LREEs) ((La/

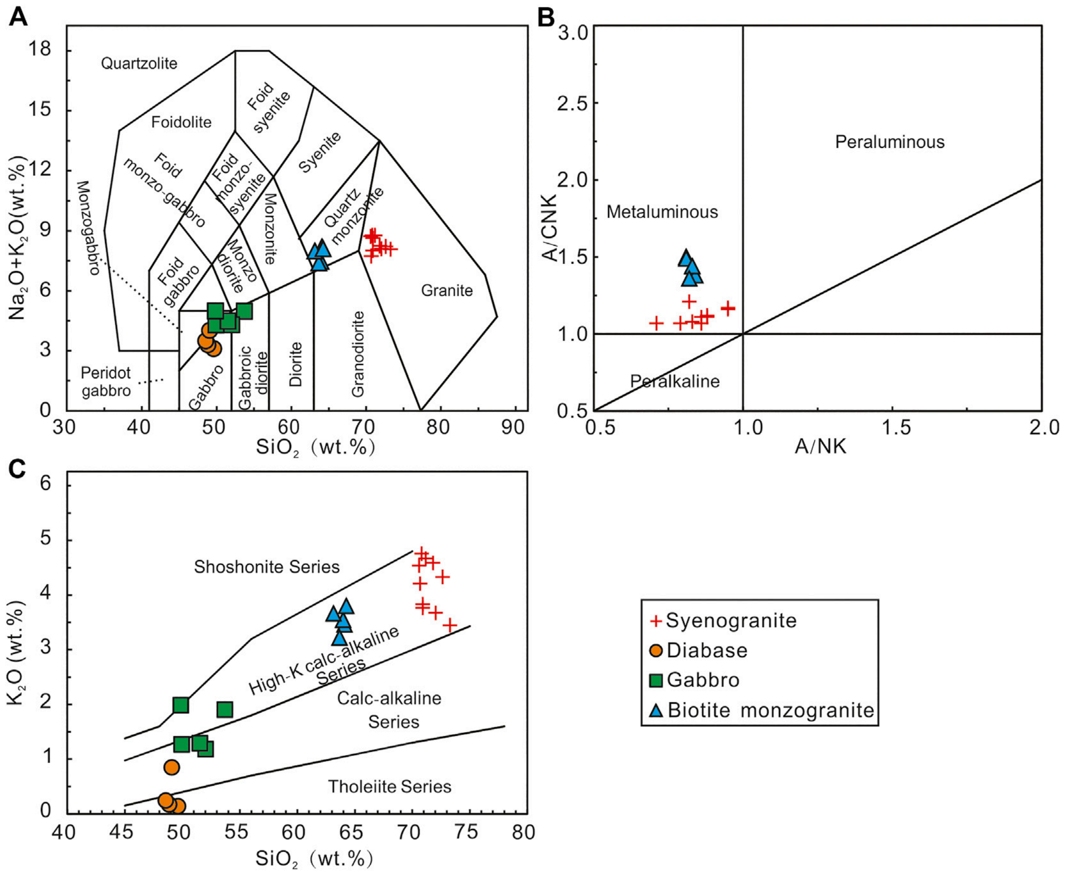

FIGURE 6
(A) Total alkali (Na_2O + K_2O) versus silica (SiO_2) diagram (Middlemost, 1994); **(B)** A/NK versus A/CNK diagram; **(C)** K_2O versus SiO_2 diagram (Rickwood, 1989).

$Yb)_N$ = 8.61–11.82) with negative Eu anomalies (δEu = 0.45–0.60) (Figure 7B).

5.2.2 Diabase

The samples (16YG3 to 16YG6 in Supplementary Table S2) have low K_2O (0.14–0.85 wt%), high Na_2O (2.97–3.25 wt%), TFe_2O_3 (11.23–11.76 wt%), and MgO (6.0–6.07 wt%, $Mg^{\#}$ = 48–49) contents. All samples plot in gabbro field and belong to diabase (Figure 6A). The diabase is characteristic of calc-alkaline series (Figure 6C). They are enriched in Rb, Sr and Ba (Figure 7C), depleted in HFSEs and exhibit enrichments in LREEs ($(La/Yb)_N$ = 2.07–2.19), with no obvious negative Eu anomalies (δEu = 0.92–0.95) (Figure 7D).

5.2.3 Gabbro

The samples (16YG12 to 16YG16 in Supplementary Table S2) have high CaO (9.84–12.68 wt%) and Al_2O_3 (14.32–15 wt %) contents, low TiO_2 (0.59–0.74 wt%) contents and high $Mg^{\#}$ values of 60–66. All samples are located in the gabbro field in the (Na_2O + K_2O) - SiO_2) diagram (Figure 6A) and belong to the calc-alkaline series to high-K calc-alkaline series (Figure 6C). They display enrichments in Pb, Rb, Sr, and K, and LREEs ($(La/Yb)_N$ = 5.56–7.10) with negative Eu anomalies (δEu = 0.78–0.85) (Figure 7F), and depletions in Nb, Ta, Ti and P (Figure 7E).

5.2.4 Biotite monzogranite

The samples (16YG7 to 16YG11 in Supplementary Table S2) fall in quartz monzogranite field and belong to quartz monzonite (Figure 6A). They are metaluminous and high-K calc-alkaline series (Figures 6B,C) and show enrichments in Rb, K, Pb, Th, and U and depletions in Nb, Ta, Ti, and Ba (Figure 7G), with slight enrichments in LREEs ($(La/Yb)_N$ = 8.58–9.23) and Eu anomalies (δEu = 0.76–0.83) (Figure 7H).

5.3 Nd-Hf isotope systems

The whole-rock Nd-Hf isotope data are listed in Supplementary Table S3.

10.3389/feart.2022.1046122

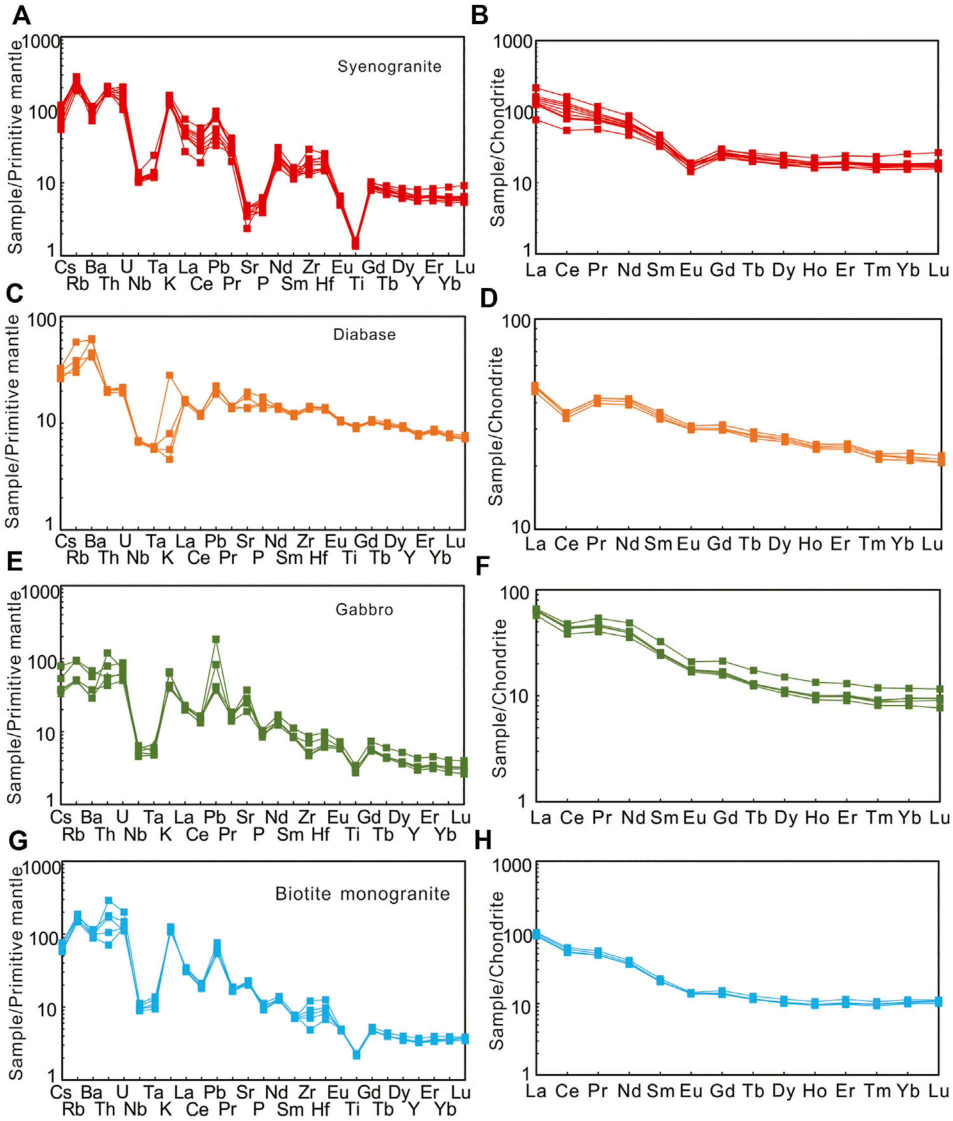

FIGURE 7
Primitive mantle normalized multi-element **(A–G)** and chondrite normalized REE patterns diagrams **(B–H)** of the syenogranites and the diabase, gabbro and biotite monzogranite. Data for chondrite and primitive are from Sun & McDonough (1989).

The four syenogranites (16 YG-01 to 16 YG-04 in Supplementary Table S3) have negative $\varepsilon_{Nd}(t)$ (t = 374.8 Ma) values (-2.1 to −1.9) (Figure 8A) and positive $\varepsilon_{Hf}(t)$ values (+0.1 - +1.1) (Figure 8B). The diabase samples (16 YG-05 to 16 YG-08 in Supplementary Table S3) have positive ε_{Nd} (t) and ε_{Hf} (t) (t = 261.4 Ma) values (+0.9 - +2.7 and +7.1 - +8.6, respectively) (Figure 8). The gabbro samples (16 YG-09 to 16 YG-12 in Supplementary Table S3) have variable ε_{Nd} (t = 262.9 Ma) values from -2.3 to 0.3 (average value of -0.1) (Figure 8A) and positive ε_{Hf} (t) values (+2.6 - +3.4) (Figure 8B). The biotite monzogranite samples (16 YG-13 to 16 YG-16 in Supplementary Table S3) have negative ε_{Nd} (t = 263.4 Ma) values (-2.6 to −2.4) (Figure 8A) and variable ε_{Hf} (t) values from -2.1–0.3 (average value of -0.5) (Figure 8B).

6 Discussion

6.1 Petrogenesis

6.1.1 The late devonian syenogranite

The late Devonian syenogranite (ca. 374.8 Ma) have the chemical features of I-type or A-type granites (metaluminous, A/CNK <1.1 and A/NK > 1) and contain no aluminum-rich

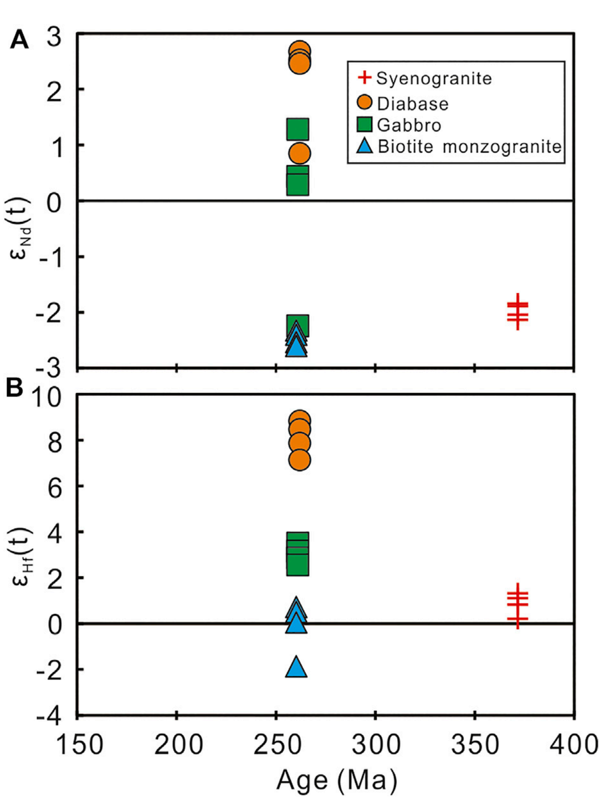

FIGURE 8
(A) ε_{Nd}(t) values of igneous rocks; **(B)** ε_{Hf}(t) values of igneous rocks.

minerals (such as garnet and muscovite) (Chappel and White, 1992). All samples have relatively high 10000 Ga/Al ratios of 2.68–3.28 and show enrichments in Rb, Th, K, and Pb and depletions in Nb, Ta, Ba, and Ti (Figure 7A), similar to those of A-type granites (Whalen et al., 1987), but they have lower Zr + Nb + Ce + Y values (245 ppm–330 ppm, except for one sample 16 YG-36 with a value of 434 ppm) than A-type granite (Zr + Nb + Ce + Y > 350 ppm, Eby, 1990). On the other hand, fractionated I-type granites usually show geochemical characteristics similar to those of A-type granites (Chappell and White, 1992). The syenogranite has high contents of SiO_2 (70.03–73.27 wt%), Na_2O (3.53–4.86 wt%), and K_2O (3.45–4.67 wt%) and low contents of CaO (1.39–3.14 wt%). Zr/Hf (30–36, except for one sample 16 YG-36 with a ratio 41) and Nb/Ta (10–16) ratios of the rocks are similar to those of highly fractionated granites (Zr/Hf < 38, Nb/Ta < 17; Wu et al., 2017), with depletions in Sr, Nb, Ta, and Ti (Figure 7A) and negative Eu anomalies (Figure 7B). Also, compared to A-type granites field, a common sample plots in the highly fractionated granites (FG) (Figure 9A). These geochemical features suggest that samples have characteristic of fractionation. With everything else, it is notable that all the syenogranite samples display an I-type granite trend such as Th vs. Rb and Y vs. Rb (Figure 9B) correlations and negative P_2O_5 vs. SiO_2 correlations (Figure 9C) (Whalen et al., 1987; Wu et al., 2017). Notably, the rocks contain small amounts of amphibole (3%) (Figure 3B), implying that they formed in a water-rich environment. Therefore, mineralogical and geochemical features suggest that the late Devonian syenogranite is an I-type granite rather than an A-type granite.

I-type granites may be generated from either partial melting of the lower crust heated by underplating of mantle-derived magma (Wu et al., 2003) or fractional crystallization of crust-mantle mixed magma (Wang et al., 2017) and of mantle-derived basaltic magma (Cribb & Barton, 1996). The depletions in Nb, Ta, and P (Figure 7A) in the syenogranite samples suggest the involvement of some crustal materials. Moreover, the syenogranite samples have low Mg# values (6.9–13.2) and Th/U (average of 5.9) and Sm/Nd (average of 0.2) ratios, which are similar to the lower crustal values (Th/U = 6, Sm/Nd = 0.25, Rudnick & Gao 2003), and they have Rb/Sr ratios (1.6–3.1) similar to those of crustal materials (>0.5, Meschede, 1986). All

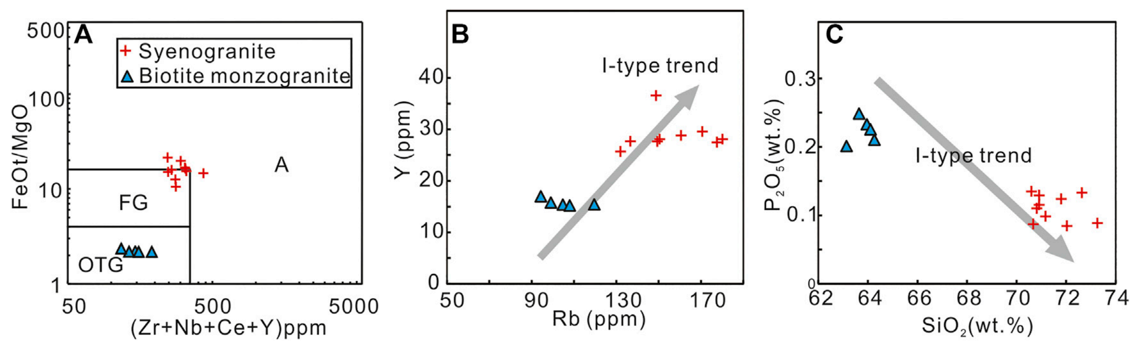

FIGURE 9
(A) K_2O/MgO versus 10000Ga/Al (Whalen et al., 1987); **(B)** Y versus Rb diagrams; **(C)** P_2O_5 versus SiO_2 diagrams. Abbreviations: FG—highly fractionated I-type granites; OTG—undifferentiated I, S, M-type granites.

10.3389/feart.2022.1046122

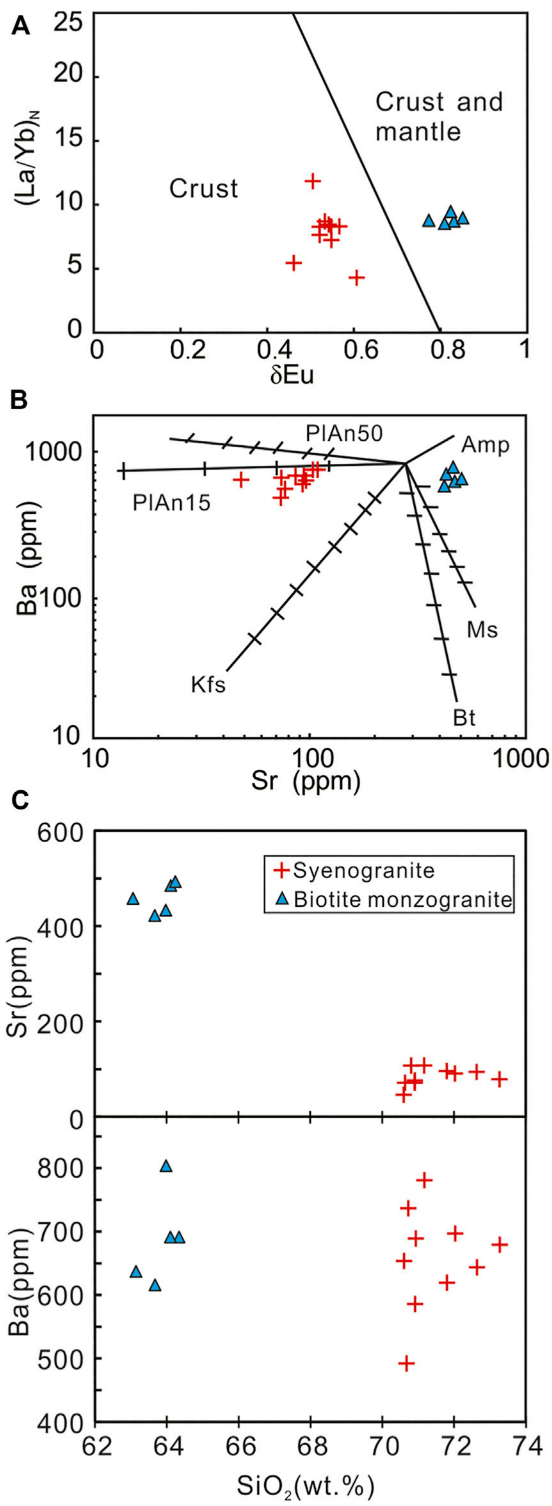

FIGURE 10
(A) $(La/Yb)_N$ versus δEu diagrams; **(B)** Ba versus Sr diagrams; **(C)** SiO_2 versus Sr and Ba. Abbreviations: Amp–amphibole; Pl–plagioclase; Kfs–K-feldspar; Bt–biotite; Ms–muscovite.

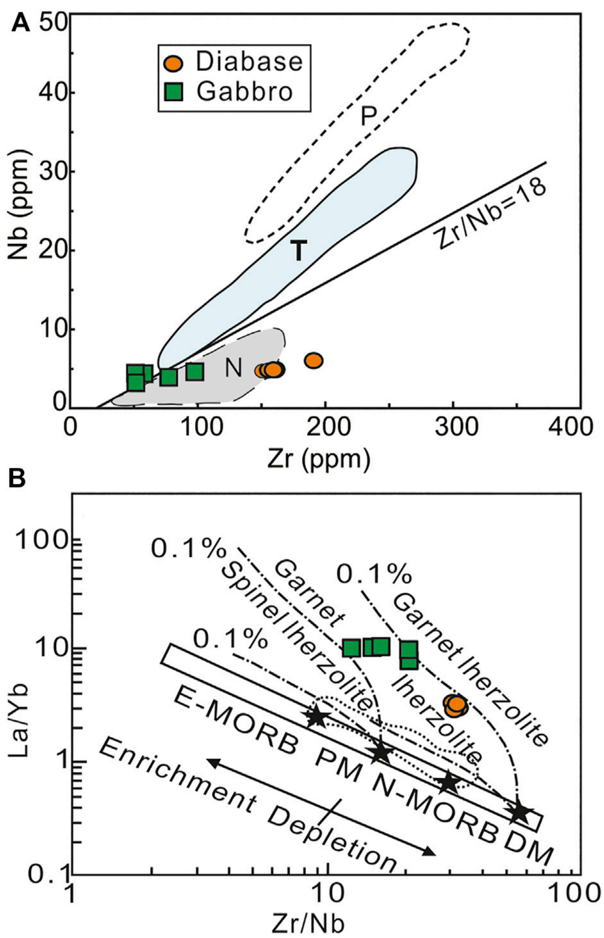

FIGURE 11
Magma source discrimination diagrams for the diabase and gabbro: **(A)** Nb versus Zr (Le Roex et al., 1983); **(B)** La/Yb versus Zr/Nb (Zhao & Zhou, 2007). N–depleted mantle; T–transitional mantle; P–primitive mantle.

sample spots are located in the crustal field on the $(La/Yb)_N$ vs. δEu diagram (Figure 10A). These features indicate that the syenogranite magma was derived mainly from a lower crustal source, and their fractionated REE patterns (Figure 7A) and obvious negative Eu anomalies (Figure 7B) may have resulted from fractional crystallization of lower crustal melts. In addition, the rocks have negative $\varepsilon_{Nd}(t)$ and positive $\varepsilon_{Hf}(t)$ values (Figure 8) and two-stage model ages (T_{DM2}) of 1300–1360 Ma, indicating that they are the product of partial melting of ancient (Mesoproterozoic) continental crust.

The syenogranite samples show depletions in Sr and Ba (Figure 7A), no significantly negative Eu anomalies (Figure 7B) and a weak fractional crystallization trend of plagioclase (Figure 10B). However, they have high Ba content, and in the diagram (Figure 10C), SiO_2 is not correlated negatively

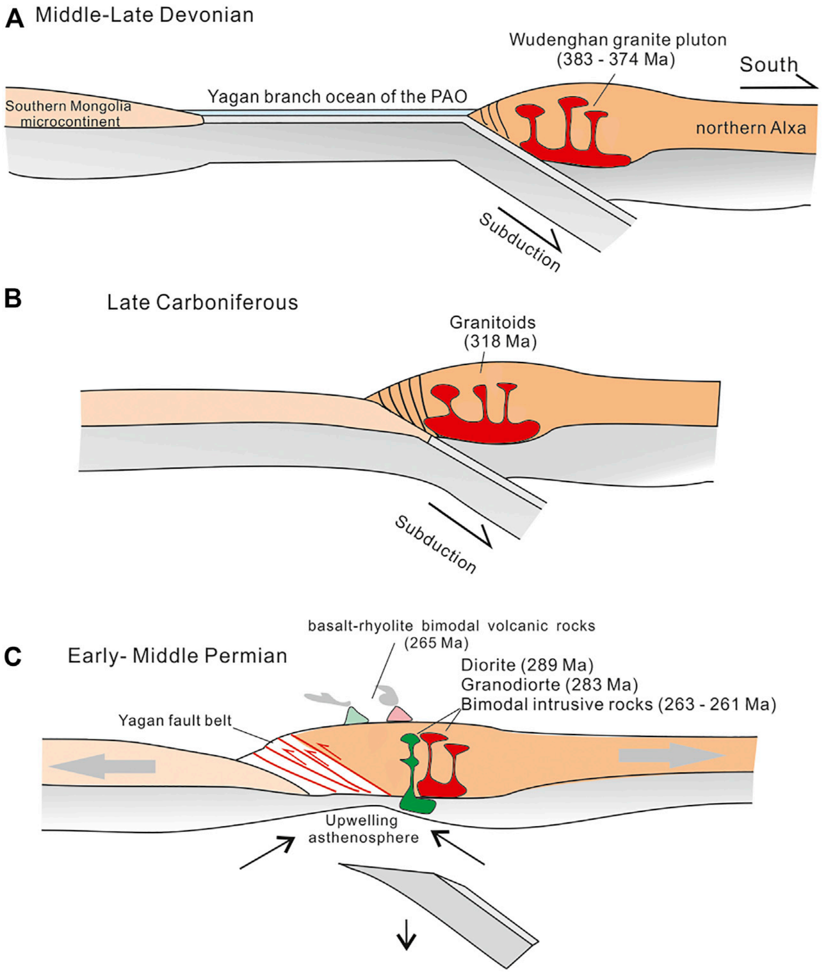

FIGURE 12
Late Paleozoic tectonic evolution model in the northern Alxa (Data: Zhang et al., 2017; Li, 2019; Xie et al., 2020; Zhao et al., 2020).

with the contents of Sr and Ba. All features indicate that the syenogranite may have experienced weak fractionation of plagioclase.

6.1.2 Middle permian bimodal intrusive rocks

The middle Permian bimodal intrusive rocks are mainly composed of diabase, gabbro and biotite monzogranite, with LA-ICP-MS zircon U-Pb ages of 261.4 Ma, 262.1 Ma, and 260.7 Ma. The diabase and gabbro have high contents of Al_2O_3, MgO, $Mg^{\#}$ and TFe_2O_3 and low contents of K_2O and P_2O_5, and belong to the calc-alkaline series (Figure 6C). They display similar geochemical characteristics (Supplementary Table S2), REE patterns (Figures 7C–F) and evolutionary trends (Figure 11). Nb/Ta ratios (19–20) for diabase, and 15.1–20.9 for gabbro are similar to mantle values (17.5 ± 2.5, Sun & McDonough, 1989). The diabase and gabbro have source features of depleted mantle (Figure 11A) and corresponding evolutionary trends (Figure 11B). Moreover, the diabase and gabbro have positive $\varepsilon_{Nd}(t)$ and $\varepsilon_{Hf}(t)$ values (Figure 8), suggesting depleted mantle (Wu et al., 2007). All of these features indicate that the diabase and gabbro were derived from the partial melting of depleted mantle.

While, the diabase and gabbro have high Ba/Nb (59–89, 49–120, respectively), Zr/Hf (36–37, 26–32, respectively) and La/Nb ratios (2.2–2.3, 3.4–4.1, respectively). They are all close to the values of the continental crustal (Ba/Nb = 54, La/Nb = 2.2, Weaver, 1991; Zr/Hf = 33, Taylor & McClennan 1995). Moreover, Their Nb/U (11–12, 1.7–3.6, respectively) and Ce/Pb ratios (5.1–5.9, 0.8–3.9, respectively) were close to values of crust (Nb/U = 8.9, Taylor & McClennan 1995; Ce/Pb < 15, Hofmann et al., 1986). The data aforementioned above imply the diabase and gabbro might experience different degrees of crustal contamination during emplacement of the magma. They show enrichments in LILEs (K, Rb, Ba), depletions in HSFEs (Nb, Ta, Ti) (Figures 7C,E) and negative Ce anomalies (Figures 7D,F),

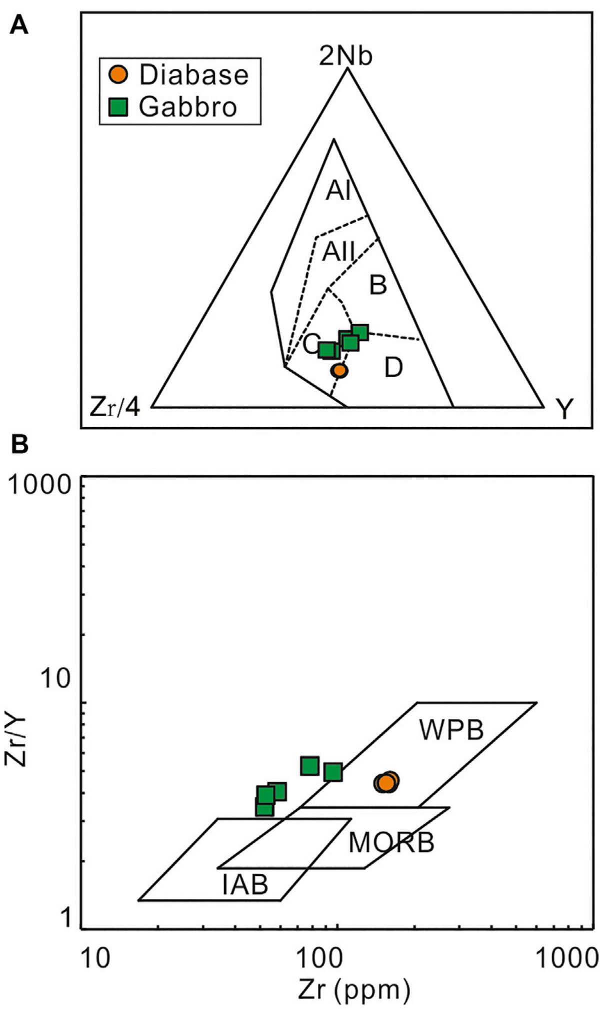

FIGURE 13
Tectonic environment discrimination diagrams for the diabase and gabbro: **(A)** 2Nb−Zr/4−Y (Meschede, 1986); **(B)** Zr/Y versus Zr (Pearce & Norry, 1979). MORB−mid-ocean ridge basalts; IAB−island-arc basalts; WPB−within plate basalts; AI−within plate alkaline basalts; AII−tholeiite and within plate tholeiite; B−mid-ocean ridge basalts; C−within plate basalts and volcanic arc basalts; D−volcanic arc basalts and normal mid-ocean ridge basalts.

perhaps resulting from crustal contamination (Li et al., 2003). These features imply that crustal contamination played a significant role in the petrogenesis of the diabase and gabbro. The gabbro and diabase have positive Sr anomalies (Figures 7C,E) and slightly negative Eu anomalies (Figures 7D,F), indicating no fractional crystallization of plagioclase during magmatism or the remains of relics of plagioclase in the magma source (Goss et al., 2010).

The Middle Permian biotite monzogranites have high K_2O, Na_2O, and CaO contents and low P_2O_5 contents and belong to the high-K calc-alkaline series (Figure 6C). Their A/CNK (0.81–0.84) and A/NK ratios (1.36–1.50) are similar to those of I-type granites (A/CNK <1.1 and A/NK > 1, Whalen et al., 1987). Additionally, they have amphibole inclusions (Figure 3K and L) and show enrichments in LREEs (Figure 7G) and weakly negative Eu anomalies (Figure 7H), being characteristic of I-type granites. The biotite monzonite samples plot in the I-type granite (Figure 9A) and Y vs. Rb for the rocks have positive correlation (Figure 9B) and a P_2O_5 vs. SiO_2 negative correlation (Figure 9C), showing some characteristic of an I-type granite trend. Therefore, we infer that the biotite monzogranites are I-type granites.

Bimodal igneous rocks are generally assumed to have two petrogenesis characteristics (Davies & MacDonald, 1987; Zhang et al., 2021). The diabase, gabbro and biotite monzogranite have similar patterns (Figure 7), but the trace element contents and whole-rock Nd-Hf isotopes vary widely (Supplementary Table S3). In addition, the biotite monzogranite outcrop area is larger than the diabase and gabbro area (Figure 2B). Therefore, we consider that diabase and biotite monzogranite have different magma sources. The origins of granitic magma are mainly divided into mantle-sourced magma the lower crust (Whalen et al., 1987) and partial melting of crustal materials heated by basalt magma underplating (Wu et al., 2003). The biotite monzonites have high contents of SiO_2, K_2O, and Na_2O and low contents of P_2O_5 and show depletions in Nb, Ta, Ti, P and Sr and enrichments in Zr and Hf (Figure 7G), with negative $\varepsilon_{Nd}(t)$ values (Figure 8A), indicating partial melting of lower crustal materials (Jiang et al., 2013). However, their Nb/Ta ratios (10–16) are between the depleted mantle (17.7, Sun & McDonough, 1989) and the lower crust values (8.3, Rudnick & Gao, 2003), and they have various $\varepsilon_{Hf}(t)$ values (Figure 8B) and moderate $Mg^{\#}$ values (40–43), indicating the characteristics of crust-sourced magma mixed by mantle-sourced underplating magma. In addition, these samples plot in the crust-mantle mixing region and show low Rb/Sr ratios (0.2–0.3) (crust-mantle = 0.05–0.5, Meschede, 1986). These features also support the above conclusion. Therefore, we consider that the middle Permian biotite monzogranites were generated from the product of partial melting of lower crust heated, and then mixed by mantle-derived magma underplating. The biotite monzogranites show positive Sr anomalies (Figure 7G) and lightly negative Eu anomalies (Figure 7H; δEu = 0.76–0.83), and the correlation of SiO_2 with the contents of Sr and Ba does not follow a linear trend (Figure 10C), implying no obvious crystallization of plagioclase during emplacement processes of acid magma (Figure 10B).

6.2 Tectonic implications

The tectonic evolution of northern Alxa during the late Paleozoic is controversial. Many geological evidences show the northern Alxa has undergone multiple phases of tectonic evolution from subduction (Zhao et al., 2020), collision to post-collision (Xie et al., 2020) during late Devonian to middle Permian. Usually, magmatic activity is an important indicator for the analysis of regional tectonics (Han et al., 2007). Late Paleozoic igneous rocks are of key significance for defining the tectonic setting in northern Alxa. The late Devonian syenogranites belong to the high-K calc-alkaline series and I-type granites in this paper. They show enrichments in Rb, K, Th, and depletions in Nb, Ta, Ti, and P (Figure 7A), indicating island arc characteristics related to subduction zones. The spider diagram of trace element ratio and the REE distribution patterns show the characteristics of the island arc calc alkaline series (Batcher and Bowden, 1985; Woodhead et al., 1998). These features suggest that the syenogranite should form in a volcanic arc setting that is, continental margin arc.

By combining these findings with the lithostratigraphy characteristics, some ideas can be inferred. 1) Early Paleozoic sedimentary strata are widely distributed, and the sedimentary package is continuous in northern Alxa (Wu & He, 1993; Yin, 2016). They are mainly composed of Cambrian-Silurian siliceous rocks of the Xishuangyingshan and Bandingtaolegai Formations and are considered to represent an archipelagic ocean environment, implying a stable marine deposit setting (Zheng et al., 2017). The middle Devonian strata are mainly limestones and sandstones comprising the Wotuoshan Formation. The Upper Devonian strata are mainly volcaniclastic rocks of the Xipingshan Formation in the ZHTZ, reflecting magmatic activity related to the subduction of the ocean basin (Zhang et al., 2017). The Carboniferous strata have an unconformable contact with the Devonian strata (Zhang et al., 2018). These stratigraphic features indicate uplift denudation caused by orogenic events during the late Devonian - Carboniferous. 2) The late Devonian magmatic activity is characterized by a volcanic arc in the ZHTZ. The Late Devonian Wudenghan monzogranite (383 Ma, Figure 2) is a calc-alkaline series and I-type granite representing volcanic arc granite (Zhang et al., 2017). The late Devonian granite and diorite (373 Ma, Figure 2) in the Wudenghan were reported to have both volcanic and subduction setting characteristics (Zhao et al., 2020). These results are consistent with this late Devonian syenogranite (374.8 Ma). Therefore, the above sedimentary and magmatic activity confirms that the ZHTZ transformed from a passive continental margin to an active continental margin during the late Devonian.

The Enger Us ophiolite belt (Figure 1C) is regarded as the major suture zone and shows an N-MORB geochemical signature (Wang et al., 1992; Zheng et al., 2014). Previous studies have suggested that southward subduction of the PAO is represented by the Enger Us ophiolite belt and that the Quagan Qulu ophiolitic belt (Figure 1B) represents a back-arc basin (Wang et al., 1993, 1994; Wu & He, 1993; Zhang et al., 2014). Moreover, the Enger Us ophiolite belt has a series of northward imbricated thrust faults, indicating that the PAO was still subducted southward (Wang et al., 1994). However, according to magmatic activities that existed at the Yagan fault belt, the Yagan branch ocean of the PAO underwent southward subduction during the Devonian (Song, 2017). In summary, the Yagan branch ocean of the PAO began southward subduction, causing passive continental margins to become active continental margins for the ZHTZ during the Late Devonian (Figure 12A).

The late Carboniferous medium-K calc-alkaline granitoids (318 Ma, Figure 1C) are arc-related under the subduction setting in the ZHTZ (Zhao et al., 2020). Moreover, the lower Carboniferous strata are largely absent in northern Alxa, implying a strongly tectonic uplift and collision environment (Zhang et al., 2018). Outliers of gneiss and marble indicate strong metamorphism (Figure 2B). These geological events indicate that the ZHTZ remained an active continental margin during the Late Carboniferous, which means that the Yagan branch ocean closed during the late Carboniferous (Figure 12B).

The early Permian magmatic activities mainly include diorite (289.3 Ma, Figure 2, Xie et al., 2020) and the granodiorite (286 Ma, Figure 2, Zheng et al., 2017) are suggested to have formed in a post-collision extensional tectonic setting. All the above sedimentary and magmatic rocks indicate that the ZHTZ was transformed to a post-collision extensional setting during the Early Permian. These middle Permian bimodal intrusive rocks (263.4–261.4 Ma) are high-K and calc-alkaline to tholeiite (Figure 6C), which reveals that the Yagan area (Figure 2) experienced another tectono-magmatic event during the Permian. They were formed in a post-collision extensional tectonic setting. The diabase and gabbro samples plot in the within-plate basalt and volcanic arc basalt fields (Figure 13A). On the Zr/Y vs. Zr discrimination diagram (Figure 13B), all diabase samples plot in the within-plate basalt (WPB) field, and some gabbro samples plot on the boundary of the WPB area. These features suggest that the gabbro and diabase formed in a within-plate tectonic setting. The biotite monzonite samples are high-K calc-alkaline series (Figure 6C) and I-type granites, are one of the single most important magmatic process characteristics of post-collision extensional setting (Han et al., 2007). These features imply that the middle Permian bimodal intrusive rocks formed in a post-collision extensional setting. Moreover, the basalt-rhyolite volcanic rocks (265 Ma) formed in the same tectonic setting in northern Alxa (Li, 2019). All these features indicate that the ZHTZ was still in a post-collision tectonic environment during the middle Permian (Figure 12C).

7 Conclusion

1) The LA-ICP-MS zircon U-Pb dating results for late Paleozoic igneous rocks in northern Alxa are as follows: late Devonian syenogranite (ca. 374.8 Ma), middle Permian diabase (ca. 261.4 Ma), gabbro (ca. 262.9 Ma) and biotite monzogranite (ca. 263.4 Ma).
2) The late Devonian syenogranite belongs to I-type granites and was generated from partial melting of the crust in an active continental margin setting. The middle Permian diabase and gabbro were derived from depleted mantle. The middle Permian biotite monzogranite is an I-type granite and was generated by crust-mantle mixing. The diabase, gabbro and biotite monzogranite all formed in the post-collision extensional setting.
3) The ZHTZ was an active continental margin during the late Devonian linking to southward subduction of the Yagan branch ocean of the PAO which finally closed before the middle Permian.

Data availability statement

The original contributions presented in the study are included in the article/Supplementary Material, further inquiries can be directed to the corresponding author.

Author contributions

E-TW: Investigation, Conceptualization, Methodology, Software, Data curation, Formal analysis, Writing—original draft, Writing—review and editing, Project administration. X-WZ: Project administration, Investigation, Writing—review and editing. W-FC: Investigation, Methodology. ZM: Investigation, Formal analysis. LW: Writing—review and editing. Z-AG: Investigation, Formal analysis. YW: Investigation, Formal analysis. G-RS: Investigation, Formal analysis. J-RW: Project administration, Funding acquisition.

Funding

This work is supported by the National Second Expedition to the Tibetan Plateau (2019QZKK0901) and the China Geological Survey (No. 121201011000161111-01).

Acknowledgments

We are grateful to professorial senior engineers Jincai Lu and Yazhuo Niu of Xian Geological Survey Center of China Geological Survey for the help during the field geological survey. Many thanks for two reviewers and editor Zhong-Hai Li, which greatly helped to improve the manuscript.

Conflict of interest

The authors declare that the research was conducted in the absence of any commercial or financial relationships that could be construed as a potential conflict of interest.

Publisher's note

All claims expressed in this article are solely those of the authors and do not necessarily represent those of their affiliated organizations, or those of the publisher, the editors and the reviewers. Any product that may be evaluated in this article, or claim that may be made by its manufacturer, is not guaranteed or endorsed by the publisher.

Supplementary material

The Supplementary Material for this article can be found online at: https://www.frontiersin.org/articles/10.3389/feart.2022.1046122/full#supplementary-material.

References

Andersen, T. (2002). Correction of common lead in U–Pb analyses that do not report 204Pb. *Chem. Geol.* 192, 59–79. doi:10.1016/s0009-2541(02)00195-x

Batchelor, R. A., and Bowden, P. (1985). Petrogenetic interpretation of granitoid rock series using multicationic parameters. *Chem. Geol.* 48, 43–55. doi:10.1016/0009-2541(85)90034-8

Chappell, B. W., and White, A. J. R. (1992). I- and S-type granites in the lachlan fold belt. *Earth Environ. Sci. Trans. R. Soc. Edinb.* 83, 1–26. doi:10.1017/s0263593300007720

Cribb, J. W., and Barton, M. (1996). Geochemical effects of decoupled fractional crystallization and crustal assimilation. *Lithos* 37 (4), 293–307. doi:10.1016/0024-4937(95)00027-5

Dan, W., Li, X., Wang, Q., Tang, G., and Liu, Y. (2014). An early permian (ca. 280Ma) silicic igneous province in the Alxa block, NW China: A magmatic flare-up triggered by a mantle-plume? *Lithos* 204, 144–158. doi:10.1016/j.lithos.2014.01.018

Davies, G. R., and Macdonald, R. (1987). Crustal influences in the petrogenesis of the Naivasha basalt-comendite complex: Combined trace element and Sr-Nd-Pb isotope constraints. *J. Petrology* 28, 1009–1031. doi:10.1093/petrology/28.6.1009

Eby, G. N. (1990). The A-type granitoids: A review of their occurrence and chemical characteristics and speculations on their petrogenesis. *Lithos* 26, 115–134. doi:10.1016/0024-4937(90)90043-z

Fei, M. M., Pan, M., Xie, C. L., Wang, J. H., and Zhao, H. S. (2019). Timing and tectonic settings of the late paleozoic intrusions in the Zhusileng, northern Alxa: Implication for the metallogeny. *Geosci. J.* 23, 37–57. doi:10.1007/s12303-018-0018-z

Goss, S. C., Wilde, S. A., Wu, F. Y., and Yang, J. H. (2010). The age, isotopic signature and significance of the youngest mesozoic granitoids in the Jiaodong terrane, Shandong province, north China craton. *Lithos* 120, 309–326. doi:10.1016/j.lithos.2010.08.019

Han, B. F. (2007). Diverse post-collisional granitoids and their tectonic setting discrimination. *Earth Sci. Front.* 14, 064–072.

Hofmann, A. W., Jochum, K. P., Seufert, M., and White, W. M. (1986). Nb and Pb in oceanic basalts: New constraints on mantle evolution. *Earth Planet. Sci. Lett.* 79, 33–45. doi:10.1016/0012-821x(86)90038-5

Hui, J., Zhang, K., Zhang, J., Qu, J., Zhang, B., Zhao, H., et al. (2021). Middle-late Permian high-K adakitic granitoids in the NE Alxa block, northern China: Orogenic record following the closure of a Paleo-Asian oceanic branch? *Lithos* 402-400, 106379. doi:10.1016/j.lithos.2021.106379

Jahn, B. M., Wu, F. Y., and Chen, B. (2000). Granitoids of the central asian orogenic belt and continental growth in the phanerozoic. *Earth Environ. Sci. Trans. R. Soc. Edinb.* 91, 181–193. doi:10.1017/s0263593300007367

Jiang, N., Guo, J., and Chang, G. (2013). Nature and evolution of the lower crust in the eastern north China craton: A review. *Earth-Science Rev.* 122, 1–9. doi:10.1016/j.earscirev.2013.03.006

LeRoex, A. P., Dick, H. J. B., Erlank, A. J., Reid, A. M., Frey, F. A., and Hart, S. R. (1983). Geochemistry, mineralogy and petrogenesis of lavas erupted along the southwest Indian ridge between the bouvet triple junction and 11 degrees east. *J. Petrology* 24, 267–318. doi:10.1093/petrology/24.3.267

Li, H., Zhou, J., and Wilde, S. A. (2022). Nature and development of the South Tianshan-Solonker suture zone. *Earth-Science Rev.* 233, 104189. doi:10.1016/j.earscirev.2022.104189

Li, R. W., Zhang, X., Shi, Q., Chen, W. F., An, Y., Huang, Y. S., et al. (2020). Early permian to late triassic tectonics of the southern central asian orogenic belt: Geochronological and geochemical constraints from gabbros and granites in the northern Alxa area, NW China. *Geol. Mag.* 157, 2089–2105. doi:10.1017/s0016756820000345

Li, S., Wang, T., Wilde, S. A., and Tong, Y. (2013). Evolution, source and tectonic significance of Early Mesozoic granitoid magmatism in the Central Asian Orogenic Belt (central segment). *Earth-Science Rev.* 126, 206–234. doi:10.1016/j.earscirev.2013.06.001

Li, X. H., Chen, Z. G., Liu, D. Y., and Li, W. X. (2003). Jurassic gabbro-granite-syenite suites from southern jiangxi province, SE China: Age, origin, and tectonic significance. *Int. Geol. Rev.* 45, 898–921. doi:10.2747/0020-6814.45.10.898

Li, Y. Q. (2019). *Master thesis*. Lanzhou, China: Lanzhou University.Geochemistry of volcanic rocks in the jinta formation of north to Alxa block and its tectonic implications

Liang, X. R., Wei, G. G., Li, X. H., and Liu, Y. (2002). Rapid and precise measurement for 143Nd/144Nd isotopic ratios using a multi-collector inductively coupled plasma mass spectrometer. *Rock and Mineral Analysis* 24, 247–251 (in Chinese with English abstract). doi:10.15898/j.cnki.11-2131/td.2002.04.002

Liu, Q., Zhao, G. C., Han, Y., Eizenhöfer, P. R., Zhu, Y. L., Hou, W. Z., et al. (2017). Geochronology and geochemistry of Permian to Early Triassic granitoids in the Alxa Terrane: Constraints on the final closure of the Paleo-Asian Ocean. *Lithosphere* 9 (4), 665–680. doi:10.1130/L646.1

Liu, Q., Zhao, G. C., Han, Y., Li, X. P., Zhu, Y. L., Eizenhöfer, P. R., et al. (2018). Geochronology and geochemistry of paleozoic to mesozoic granitoids in western inner Mongolia, China: Implications for the tectonic evolution of the southern central asian orogenic belt. *J. Geol.* 126, 451–471. doi:10.1086/697690

Luan, Y., He, K., and Tan, X. J. (2019). *In situ* U- Pb dating and trace element determination of standard zircons by LA- ICP- MS. *Geol. Bull. China* 38, 1206–1218. (in Chinese with English abstract).

Ludwig, K. R. (2003). User's manual for Isoplot 3.0: A geochronological toolkit for microsoft excel, 4. *Berkeley Geochronology Center Special Publication*, 1–71.

Meschede, M. (1986). A method of discriminating between different types of mid-ocean ridge basalts and continental tholeiites with the Nb1bZr1bY diagram. *Chem. Geol.* 56, 207–218. doi:10.1016/0009-2541(86)90004-5

Middlemost, E. A. K. (1994). Naming materials in the magma/igneous rock system. *Earth-Science Rev.* 37, 215–224. doi:10.1016/0012-8252(94)90029-9

Pearce, J. A., and Norry, M. J. (1979). Petrogenetic implications of Ti, Zr, Y, and Nb variations in volcanic rocks. *Contr. Mineral. Pet.* 69, 33–47. doi:10.1007/bf00375192

Rickwood, P. C. (1989). Boundary lines within petrologic diagrams which use oxides of major and minor elements. *Lithos* 22, 247–263. doi:10.1016/0024-4937(89)90028-5

Rudnick, R. L., and Gao, S. (2003). Composition of the continental crust. *Treatise on Geochemistry* 3, 1–64. doi:10.1016/B0-08-043751-6/03016-4

Sengör, A. M. C., Natalin, B. A., and Burtman, V. S. (1993). Evolution of the Altaid tectonic collage and Palaeozoic crustal growth in Eurasia. *Nature* 364, 299–307. doi:10.1038/364299a0

Shi, J. Z., Chen, G. C., Li, Y. H., and Jiang, T. (2011). Petrologic characteristics and sedimentary environments of permian maihanhada Formation in yagan area of ejin banner, western inner Mongolia. *Geol. Bull. China* 30, 972–982. (in Chinese with English abstract).

Song, D. F., Xiao, W. J., Windley, B. F., Mao, Q., Ao, S., Wang, H. Y. C., et al. (2021). Closure of the Paleo-Asian Ocean in the middle-late triassic (Ladinian-Carnian): Evidence from provenance analysis of retroarc sediments. *Geophys. Res. Lett.* 48, e2021GL094276. doi:10.1029/2021gl094276

Song, J. J. (2017). *Master thesis*. Beijing, China: China university of geoscience.Characteristics of late paleozoic granitearound the Yagan fault zone in northern Alxa block

Su, B. X., Qin, K. Z., Sakyi, P. A., Liu, P. P., Tang, D. M., Malaviarachchi, S. P. K., et al. (2011). Geochemistry and geochronology of acidic rocks in the Beishan region, NW China: Petrogenesis and tectonic implications. *J. Asian Earth Sci.* 41, 31–43. doi:10.1016/j.jseaes.2010.12.002

Sun, S. S., and Mcdonough, W. F. (1989). Chemical and isotopic systematics of oceanic basalts: Implications for mantle composition and processes. *Geol. Soc. Lond. Spec. Publ.* 42, 313–345. doi:10.1144/gsl.sp.1989.042.01.19

Taylor, S. R., and Mcclennan, S. M. (1995). *The continental crust: Its composition and evolution by*. Oxford: Blackwell Scientific Publications, 1–312.

Wang, T. Y., and Wu, M. B. (1993). A study on the mineralization of the Northern continental margin of North China plate Alxa region. *J. LanZhou Univ. Nat. Sci.* 29, 252–256. (in Chinese with English abstract).

Wang, T. Y., Wang, J. R., and Liu, J. K. (1994). Igneous rock associations and geochemical characteristics of volcanic arc with continental crustal basement in Zongnaishan- Shalazhashan. *Geochimica* 23, 162–172. (in Chinese with English abstract).

Wang, T. Y., Wang, J. R., and Wang, S. Z. (1992). Discovery of Enger Us ophiolite belt in northern Alxa and its tectonic significance. *J. LanZhou Univ. Nat. Sci.* 28, 194–196. (in Chinese).

Wang, Z. Z., Liu, D., Zhao, Z. D., Yan, J. J., Shi, Q. S., and Mo, X. X. (2017). The Sangri highly fractionated I-type granites in southern Gangdese: Petrogenesis and dynamic implication. *Acta Petrol. Sin.* 33, 2479–2493. (in Chinese with English abstract). doi:10.00-0569/2017/033(08)-2479-93

Weaver, B. (1991). The origin of ocean island basalt end-member compositions: Trace element and isotopic constraints. *Earth Planet. Sci. Lett.* 104, 381–397. doi:10.1016/0012-821x(91)90217-6

Whalen, J. B., Currie, K. L., and Chappell, B. W. (1987). A-Type granites: Geochemical characteristics, discrimination and petrogenesis. *Contrib. Mineral. Pet.* 95, 407–419. doi:10.1007/bf00402202

Wiedenbeck, M., Alle, P., Corfu, F., Griffin, W. L., Meier, M., Oberli, F., et al. (1995). Three natural zircon standards for U-Th-Pb, Lu-Hf, trace element and REE analyses. *Geostand. Geoanal. Res.* 19, 1–23. doi:10.1111/j.1751-908x.1995.tb00147.x

Windley, B. F., Alexeiev, D., Xiao, W. J., Kroener, A., and Badarch, G. (2007). Tectonic models for accretion of the central asian orogenic belt. *J. Geol. Soc. Lond.* 164, 31–47. doi:10.1144/0016-76492006-022

Woodhead, J. D., Eggins, S. M., and Johnson, R. W. (1998). Magma genesis in the new britain island arc: Further insights into melting and mass transfer processes. *J. Petrology* 39, 1641–1668. doi:10.1093/petroj/39.9.1641

Wu, F. Y., Jahn, B. M., Wilde, S. A., Lo, C. H., Yui, T. F., Lin, Q., et al. (2003). Highly fractionated I-type granites in NE China (I): Geochronology and petrogenesis. *Lithos* 66, 241–273. doi:10.1016/s0024-4937(02)00222-0

Wu, F. Y., Li, X. H., Zheng, Y. F., and Gao, S. (2007). Lu-Hf isotopic systematics and their application in petrology. *Acta Petrol. Sin.* 23, 185–220.

Wu, F. Y., Liu, X. C., Ji, W. Q., Wang, J. M., and Yang, L. (2017). Highly fractionated granites: Recognition and research. *Sci. China Earth Sci.* 60, 1201–1219. (in Chinese with English abstract). doi:10.1007/s11430-016-5139-1

Wu, T. R., and He, G. Q. (1993). Tectonic units and the fundamental characteristics on the northern margin of the Alxa block. *Acta Geol. Sin.* 67, 97–108.doi:10.1111/j.1755-6724.1993.mp6004001.x(in Chinese with English abstract)

Wu, T. R., He, G. Q., and Zhang, C. (1998). On paleozoic tectonics in the Alxa region, inner Mongolia, China. *Acta Geol. Sin.* 72, 256–263.

Wu, Y. B., and Zheng, Y. F. (2004). Genetic mineralogy of zircon and its constraints on U-Pb dating interpretation. *Chin. Sci. Bull.* 49, 1589–1604.doi:10.1007/BF03184122(in Chinese)

Xia, L. Q., Xu, X. Y., Li, X. G., Ma, Z. P., and Xia, Z. C. (2012). Reassessment of petrogenesis of Carboniferous–Early Permian rift-related volcanic rocks in the Chinese Tianshan and its neighboring areas. *Geosci. Front.* 3, 445–471. doi:10.1016/j.gsf.2011.12.011

Xiao, W. J., Windley, B. F., Huang, B. C., Han, M., Yuan, C., Chen, H. L., et al. (2009). End-permian to mid-triassic termination of the accretionary processes of the southern altaids: Implications for the geodynamic evolution, phanerozoic continental growth, and metallogeny of central asia. *Int. J. Earth Sci.* 98, 1189–1217. doi:10.1007/s00531-008-0407-z

Xiao, W. J., Windley, B. F., Han, C. M., Liu, W., Wan, B., Zhang, J. E., et al. (2018). Late Paleozoic to early Triassic multiple roll-back and oroclinal bending of the Mongolia collage in Central Asia. *Earth-Science Reviews* 186, 94–128. doi:10.1016/j.earscirev.2017.09.020

Xie, F., Sun, Y., Wang, L., Cao, J. Y., and Xiao, W. Z. (2020). Petrogenesis and tectonic setting of the chaheilingashun pluton, north Alxa block, NW China: Constraints from whole-rock geochemistry, zircon U–Pb ages, and Hf isotope compositions. *Arab. J. Geosci.* 13, 679. doi:10.1007/s12517-020-05658-3

Xu, B., Charvet, J., Chen, Y., Zhao, P., and Shi, G. Z. (2013). Middle Paleozoic convergent orogenic belts in western Inner Mongolia (China): framework, kinematics, geochronology and implications for tectonic evolution of the Central Asian Orogenic Belt. *Gondwana Research* 23, 1342–64. doi:10.1016/j.gr.2012.05.015

Yang, G. X., Li, Y. J., Tong, L. L., Wang, Z. P., and Si, G. H. (2020). An Early Cambrian plume-induced subduction initiation event within the Junggar Ocean: Insights from ophiolitic mélanges, arc magmatism, and metamorphic rocks. *Gondwana Res.* 88, 45–66. doi:10.1016/j.gr.2020.07.002

Yang, G. X., Li, Y. J., Xiao, W. J., and Tong, L. L. (2015). OIB-type rocks within West Junggar ophiolitic melanges: Evidence for the accretion of seamounts. *Earth-Science Rev.* 150, 477–496. doi:10.1016/j.earscirev.2015.09.002

Yin, H. Q. (2016). *Late Paleozoic sedimentary characteristics and its tectonic evolution in northern Alxa area, Inner Mongolia*. Beijing, China: Doctoral thesis, China university of geoscience.

Zhang, L., Li, B. L., Liu, L., Wang, P. X., and Li, L. (2021). Geochronology, geochemistry and geological significance of the Early Devonian bimodal intrusive rocks in Wulonggou area, East Kunlun Orogen. *Acta Petrol. Sin.* 37, 2007–2028. (in Chinese with English abstract). doi:10.18654/1000-0569/2021.07.04

Zhang, W., Pease, V., Meng, Q. P., Zheng, R. G., Wu, T. R., Chen, Y., et al. (2017). Age and petrogenesis of late Paleozoic granites from the northernmost Alxa region, northwest China, and implications for the tectonic evolution of the region. *Int. J. Earth Sci.* 106, 79–96. doi:10.1007/s00531-016-1297-0

Zhang, W., Wu, T. R., Feng, J. C., Zheng, R. G., and He, Y. G. (2013). Time constraints for the closing of the Paleo-Asian Ocean in the northern Alxa region: Evidence from wuliji granites. *Sci. China Earth Sci.* 56, 153–164. (in Chinese with English abstract). doi:10.1007/s11430-012-4435-y

Zhang, Y. X., Niu, Y. Z., Wei, J. S., Shi, J. Z., and Song, B. (2018). Chronology of the haobiru Formation in the haobiru area of northern Alxa, inner Mongolia and its geological implications. *Geol. Bull. China* 37, 51–62. (in Chinese with English abstract).

Zhao, J., and Zhou, M. (2007). Geochemistry of Neoproterozoic mafic intrusions in the Panzhihua district (Sichuan Province, SW China): Implications for subduction-related metasomatism in the upper mantle. *Precambrian Res.* 152, 27–47. doi:10.1016/j.precamres.2006.09.002

Zhao, X., Liu, C. Y., Wang, J. Q., Zhang, S. H., and Guan, Y. Z. (2020). Geochemistry, geochronology and Hf isotope of granitoids in the northern Alxa region: Implications for the late paleozoic tectonic evolution of the central asian orogenic belt. *Geosci. Front.* 11, 1711–1725. doi:10.1016/j.gsf.2020.01.009

Zheng, R. G., Li, J. Y., and Liu, J. F. (2017). The age of volcanic rocks of Amushan Formation on the northern margin of Alxa block: Evidence from zircon U-Pb data. *Geol. China* 44, 612–613. (in Chinese with English abstract). doi:10.12029/gc20170119

Zheng, R. G., Wu, T. R., Zhang, W., Feng, J. C., Xu, C., Meng, Q. P., et al. (2013). Geochronology and geochemistry of the Yagan granite in the northern margin of the Alxa block: Constraints on the tectonic evolution of the southern Altaids. *Acta Petrol. Sin.* 29, 2665–2675. (in Chinese with English abstract). doi:10.00-0569/2013/029(08)-2665-75

Zheng, R., Li, J., and Zhang, J. (2021). Juvenile hafnium isotopic compositions recording a late Carboniferous–Early triassic retreating subduction in the southern central asian orogenic belt: A case study from the southern Alxa. *Geol. Soc. Am. Bull.* 134, 1375–1396. doi:10.1130/B35991.1

Zheng, R., Wu, T., Zhang, W., Xu, C., Meng, Q., and Zhang, Z. (2014). Late Paleozoic subduction system in the northern margin of the Alxa block, Altaids: Geochronological and geochemical evidences from ophiolites. *Gondwana Res.* 25, 842–858. doi:10.1016/j.gr.2013.05.011